



Synergic regulation of crystalline phase, composition and morphology of SAPO-34 via metal assistance and in situ etching strategy

Xiaosi Zhang^{a,b}, Miao Yang^a, Dong Fan^a, Ye Wang^{a,c}, Caiyi Lou^{a,b}, Haocheng Hu^{a,b}, Bing Li^a, Peng Tian^{a,*}, Zhongmin Liu^{a,b,*}

^a National Engineering Research Center of Lower-Carbon Catalysis Technology, Dalian National Laboratory for Clean Energy, Dalian Institute of Chemical Physics, Chinese Academy of Sciences, Dalian 116023, PR China

^b University of Chinese Academy of Sciences, Beijing 100049, PR China

^c Green Catalysis Centre, College of Chemistry, Zhengzhou University, Zhengzhou 450001, PR China

ARTICLE INFO

Keywords:

SAPO-34
Metal-containing molecular sieve
Hollow morphology
MTO
Crystallization mechanism

ABSTRACT

SAPO-34 with low silica content and good mass transfer property is highly desired catalytic material for syngas-to-olefins and methanol-to-olefins (MTO) reactions. However, the synthesis of low-silica SAPO-34 by common low-cost template remains a challenge as the product is always bothered by impurity contamination or CHA/AEI intergrowth. Here, a metal assistance (Me = Zn, Mg, Co, Mn) and in situ etching strategy was developed to allow the construction of hollow low-silica SAPO-34, which exhibited long catalytic lifespan and ultra-high ethylene plus propylene selectivity (86.9 wt%) in MTO reaction. The crystallization process was studied by monitoring the evolution of a Zn-containing low-silica gel with triethylamine (TEA) as the template. It was revealed that Zn atoms were more active than Si atoms to participate in the nucleation of ZnAPSO-34, which effectively inhibited the CHA/AEI intergrowth. ZnAPSO-34@SAPO-34 was obtained with further crystallization. The selective etching of Zn-containing components occurred in subsequent cooling stage owing to inhomogeneous distribution of framework T atoms, leading to the hollow low-silica SAPO (Si/(Si + Al + P) \approx 0.07 in mole) with pure CHA phase. This work provides a facile approach for the synergic regulation of crystal phase, composition and morphology of SAPO materials.

1. Introduction

Molecular sieves with well-defined microporous channels, tunable acidity and good (hydro)thermal stability are efficient shape-selective catalysts, which have found wide applications in petrochemical industry, coal chemical industry and emerging biorefineries [1–3]. The catalytic properties of molecular sieves have been demonstrated to be determined by their topologies, compositions and morphologies [4–10]. It would be highly desirable to develop strategies to realize the synergic control of specific molecular sieves with targeted compositions and morphologies, as the former is closely related with the acidity of the materials and the latter strongly affects the mass transfer properties. Nevertheless, conventional morphology control strategies using mesoporegens/modifiers often narrow the synthetic phase region of molecular sieves [11–13], making the synergic control of compositions and

morphologies a challenging work.

SAPO-34 with three dimensional 8-MR channels and large cages [14] represents one of the most attractive molecular sieves, which has exhibited excellent catalytic performance in reactions such as methanol-to-olefins (MTO) [15–17], syngas to olefins [18–20] and selective catalytic reduction of NO_x by NH₃ (NH₃-SCR) [21–23], etc. The successful industrialization of MTO process with SAPO-34 as the main active component in 2010 further aroused great research interests into the targeted synthesis, morphology control and catalysis of SAPO-34 [24]. It has been demonstrated that SAPO-34 with low Si content (low acid density) and nanosized crystallites can restrain side reactions, enhance mass diffusion and reduce coking rate, leading to an improved MTO catalytic performance [15]. However, green and economic synthesis approach to the targeted SAPO-34 catalyst for MTO reaction hitherto remains an open challenge. This is because the synthesis of low-silica

* Corresponding authors at: National Engineering Research Center of Lower-Carbon Catalysis Technology, Dalian National Laboratory for Clean Energy, iChem (Collaborative Innovation Center of Chemistry for Energy Materials), Dalian Institute of Chemical Physics, Chinese Academy of Sciences, Dalian 116023, PR China (Z. Liu).

E-mail addresses: tianpeng@dicp.ac.cn (P. Tian), zml@dicp.ac.cn (Z. Liu).

<https://doi.org/10.1016/j.cej.2024.151101>

Received 14 January 2024; Received in revised form 15 March 2024; Accepted 7 April 2024

Available online 9 April 2024

1385-8947/© 2024 Elsevier B.V. All rights reserved.

SAPO-34 ($\text{Si}/(\text{Si} + \text{Al} + \text{P}) \leq 0.07$ in mole) by using regular low-cost templates such as triethylamine (TEA) is always contaminated by impurities (SAPO-5, SAPO-11, etc.) or intergrown with AEI phase [25–30]. Both cases cause an obvious decrease of the selectivity towards ethylene and propylene.

With the aim to realize rational synthesis and property tuning of SAPO materials, considerable efforts have been devoted to understanding the nucleation and crystal growth mechanisms of SAPO-34 [31–36]. Our recent work revealed that small fragments containing Si-O-Al bonds are critical species for the nucleation and fast crystallization of SAPO-34 [37,38]. The strong interactions between the negative Si-O-Al fragments and template cations are believed to guide the formation of initial nuclei. Meanwhile, previous works have shown that MeAPO-34 (Me = Zn, Co, Mg, etc.) can be readily synthesized using TEA template without the presence of Si atoms [39–42], which implies that the incorporation of metal atoms and the formation of negative Me-O-P fragments can help TEA to direct the formation of CHA structure without its intergrowth with AEI phase. These results suggest that metal assistance may provide an effective way to facilitate the crystallization of SAPO-34 in a TEA-templated low-silica system.

In this work, a metal assistance and in situ etching strategy was developed to realize the facile synthesis of SAPO-34 with pure CHA phase, low silica content and hollow morphology (wall thickness of 100–300 nm) by using a TEA template. The moderate acidity and good mass transfer properties of the resultant SAPO-34 lead to a superior light olefins selectivity (86.9 wt%) and prolonged catalytic lifetime in MTO reaction. A detailed investigation of crystallization process based on a Zn-containing system was conducted to elucidate the effect of metal assistance and the selective etching mechanism of metal-containing components. Moreover, multiple metals were demonstrated to be effective for the strategy and the mother liquid of synthesis can be recycled.

2. Experimental section

2.1. Chemical reagents

The chemical reagents used include phosphoric acid (H_3PO_4 , 80 wt%, Sichuan Xianfeng Chemical Co.), silica sol (SiO_2 , 27.7 wt%, Shenyang Chemical Co.), pseudoboehmite (Al_2O_3 , 67.5 wt%, Shandong Chemical Co.), distilled water, triethylamine (TEA, $\text{N}(\text{CH}_2\text{CH}_3)_3$, 99 wt%), zinc oxide (ZnO, 99 wt%), magnesium acetate ($\text{Mg}(\text{CH}_3\text{COO})_2$, 99 wt%), manganese acetate ($\text{Mn}(\text{CH}_3\text{COO})_2$, 99 wt%), nickel acetate ($\text{Ni}(\text{CH}_3\text{COO})_2$, 98 wt%), cobalt acetate ($\text{Co}(\text{CH}_3\text{COO})_2$, 99.5 wt%). TEA and all transitional metal sources were obtained from Tianjin Damao Chemical Reagent Co. All the chemicals were commercial suppliers and used directly without further purification.

2.2. Synthesis of hollow low-silica SAPO-34

The typical synthesis procedure was carried out from a gel with molar composition of 3 TEA: 1 P_2O_5 : 1 Al_2O_3 : 0.25 SiO_2 : 0.02 ZnO: 50 H_2O . Pseudo-boehmite, distilled water, phosphoric acid, silica sol, TEA and ZnO were sequentially added into a plastic beaker. The resulting mixture was stirred at room temperature for 30 min to form a homogeneous gel. After further addition of ball-milled SAPO-34 seed (1.5 wt%, relative to the inorganic oxide in the initial gel) [43], the mixture was transferred into a stainless-steel autoclave and sealed quickly. The autoclave was then transferred into an oven and kept for a three-stage crystallization period under rotation (40 rpm). For the first stage, the oven was heated from room temperature to 160 °C with a heating rate of 1 °C/min, and maintained for 15 h. Then, the oven was heated from 160 °C to 200 °C with a heating rate of 1 °C/min, and maintained for 12 h. For the third stage, the heating was stopped, and the oven door was opened to allow cooling of autoclaves to room temperature (2 h). Afterwards, the product was washed and dried at 110 °C overnight. The

product was named $\text{SP}_{0.02\text{Zn}}$. The precursor of $\text{SP}_{0.02\text{Zn}}$ (without the etching stage) was named $\text{SP}_{0.02\text{Zn-P}}$, which was obtained by quickly cooling after crystallization at 200 °C. The detailed crystallization procedure is illustrated in Fig. 1.

The mother liquid can be collected and reused to synthesize another batch of hollow low-silica SAPO-34. The crystallization procedure and gel composition were the same as those of $\text{SP}_{0.02\text{Zn}}$ except the partial replacement of organic and inorganic sources by mother liquid. The product was named $\text{SP}_{0.02\text{Zn-MLRecycle}}$.

2.3. Synthesis of reference SAPO-34 samples

Without the assistance of ZnO: The syntheses were the same as the sample in 2.2 except the absence of ZnO addition (Fig. 1). The product was named $\text{SP}_{0\text{Zn}}$. The precursor of $\text{SP}_{0\text{Zn}}$ (without the etching stage) was named $\text{SP}_{0\text{Zn-P}}$.

Without the low-temperature crystallization stage: The syntheses were the same as the sample in 2.2 except the absence of the crystallization at 160 °C (Fig. 1). The product was named $\text{SP}_{0.02\text{Zn-200}}$.

Without the low-temperature crystallization stage and the assistance of ZnO: The syntheses were the same as the sample in 2.2 except the absence of the crystallization at 160 °C and ZnO addition (Fig. 1). The product was named $\text{SP}_{0\text{Zn-200}}$.

SAPO-34 with different Zn contents: The synthesis of ZnAPSO-34 with 0.8 wt% Zn content was the same as that in 2.2 except the addition of 0.03 ZnO and without the III stage (Fig. 1). The synthesis of ZnAPSO-34 with 1.7 wt% Zn content was the same as that in 2.2 except the addition of 0.03 ZnO and the absence of the II and III stages (Fig. 1).

2.4. Synthesis of hollow low-silica SAPO-34 by using other metal sources

For the synthesis of hollow low-silica SAPO-34 by using other metal sources, the crystallization procedure and gel molar composition were the same as those of $\text{SP}_{0.02\text{Zn}}$ except the replacement of ZnO by other metal sources. The product was named $\text{SP}_{0.02\text{Me}}$ (Me refers to the metal type).

2.5. Characterization

The powder X-ray diffraction (XRD) data used for the phase identification were collected from powder as-made samples using a PANalytical X'Pert PRO X-ray diffractometer with the Cu $\text{K}\alpha$ radiation ($\lambda = 1.54059 \text{ \AA}$), operating at 40 kV and 40 mA. The crystal morphology was observed using a scanning electron microscope (Hitachi SU8020). Transmission electron microscopy (TEM) images were recorded with a JEM-2100 electron microscope. The bulk compositions of samples were determined with Philips Magix-601 X-ray fluorescence (XRF) spectrometer. X-ray photoelectron spectroscopy (XPS) measurements were conducted on a Thermo ESCALAB 250Xi XPS instrument. The X-ray excitation was provided by a monochromatic Al $\text{K}\alpha$ (1486.6 eV, 15 kV, 10.8 mA) source. The surface atomic concentrations were determined from the photoelectron peak areas of Si 2p, Al 2p, P 2p and Zn 2p. The textural properties of the calcined samples were measured by N_2 sorption at $-196 \text{ }^\circ\text{C}$ on a Micromeritics ASAP2020 volumetric adsorption analyzer. Prior to the measurement, the sample was degassed at 350 °C under vacuum for 4 h. The total surface area was evaluated based on the BET equation. The micropore surface area and micropore volume were calculated using the t-plot method. The acid properties of H-form zeolites were determined by NH_3 -TPD on a Micromeritics 2920 chemical adsorption instrument. Each sample (40–60 mesh, 200 mg) was loaded into a quartz U-shaped reactor and pretreated at 600 °C for 1 h in flowing He. After the pretreatment, the sample was cooled to 100 °C and saturated with NH_3 . Then, NH_3 -TPD was carried out under a constant flow of He (20 mL min^{-1}) from 100 to 600 °C at a heating rate of $10 \text{ }^\circ\text{C min}^{-1}$. A Bruker Tensor 27 spectrometer (MCT detector) was adopted for the measurement of Fourier transform infrared spectra (FTIR). The

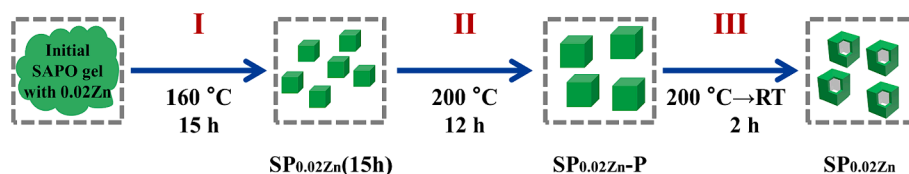


Fig. 1. Synthesis procedure of hollow low-silica SAPO-34 by metal assistance and in situ etching strategy.

samples were pressed self-supported wafers and placed into the in-situ quartz cell. Subsequently, the wafers were dehydrated at 350 °C in a vacuum for 30 min to remove adsorbed water and other molecules. After cooling to room temperature, the spectra were collected by a MCT detector in the range of 400–4000 cm^{-1} with a resolution of 4 cm^{-1} . Thermal gravimetric analyses (TG-DSC) were carried out on NETZSCH ATS 449 F3 analyzer from room temperature to 900 °C with a heating rate of 10 °C min^{-1} in an air flow of 20 mL min^{-1} .

The uptakes of propane on the SAPO-34 catalysts were carried out by intelligent gravimetric analyzer (IGA) equipped with a mesh type sample cell. The SAPO-34 catalyst (30.0 mg) was added to the chamber and evacuated at 450 °C for 4 h. The increase in mass with the adsorption of propane over SAPO-34 was measured at 40 °C (0 → 5 mbar). Fick's second law was used to quantify the effective diffusivity, and the variation of the propane concentration with time inside the SAPO-34 catalysts can be described as follows [44–46]

$$\frac{\partial C}{\partial t} = D_{\text{eff}} \left(\frac{\partial^2 C}{\partial x^2} \right) \quad (1)$$

Where x , t , C and D_{eff} represent the diffusion distance, diffusion time, propane concentration inside the particle, and the diffusivity, respectively. In the initial stage of uptake, the solution of this equation can be approximated as follows:

$$\frac{m_t}{m_\infty} = \frac{2}{\sqrt{\pi}} \sqrt{\frac{D_{\text{eff}}}{L^2}} \sqrt{t} \quad (2)$$

Where L , t and m_t/m_∞ are the characteristic diffusion length, diffusion time and the normalized propane uptake, respectively.

The solid-state NMR experiments were performed at a wide-bore 11.7 T superconducting magnet on a Bruker Avance NEO 500 spectrometer. The ^{29}Si MAS NMR spectra were recorded at a spinning rate of 8 kHz using high-power proton decoupling with a $\pi/4$ pulse width of 2.5 μs and a 10 s recycle delay. The chemical shifts were referenced to Kaolinite at -91.5 ppm. The ^{27}Al MAS NMR spectra were recorded at a spinning rate of 12 kHz using one pulse sequence. 200 scans were accumulated with a $\pi/8$ pulse width of 0.75 μs and a 2 s recycle delay. Chemical shifts were referenced to $\text{NH}_4\text{Al}(\text{SO}_4)_2 \cdot 12 \text{H}_2\text{O}$ at -0.4 ppm. The ^{31}P MAS NMR spectra were recorded with a spinning rate of 12 kHz using high-power proton decoupling. 64 scans were accumulated with a $\pi/4$ pulse width of 2.4 μs and a 10 s recycle delay. Chemical shifts were referenced to 85 % H_3PO_4 at 0 ppm.

2.6. Catalytic evaluation

The catalytic performance of the samples in the MTO reaction was tested in a quartz tubular fixed-bed reactor under atmospheric pressure. Typically, 0.3 g of calcined catalyst (40–60 mesh) was loaded in the quartz reactor and activated under a nitrogen flow at 550 °C for 1 h. After cooling to reaction temperature of 450 °C, methanol was fed by switching the carrier gas to pass through methanol saturator giving a methanol weight hourly space velocity (WHSV) of 3.65 h^{-1} . The products were analyzed by an online gas chromatograph (Agilent GC 7890 N) equipped with a flame ionization detector (FID) and a Plot-Q column. The amount of generated coke in catalysts after the MTO reactions was determined by thermal analysis on a TA SDTQ600 analyzer at a heating

rate of 10 °C min^{-1} from room temperature to 900 °C under air flow.

3. Results and discussion

3.1. Synthesis, characterization and MTO results

Hollow low-silica SAPO-34 ($\text{SP}_{0.02\text{Zn}}$) was synthesized by a ZnO assistance and in situ etching strategy, which involved the use of cost-effective TEA as OSDA and three-stage variable temperature crystallization. As shown in Table 1 and Fig. 2, $\text{SP}_{0.02\text{Zn}}$ possesses pure CHA phase in high crystallinity. For reference sample $\text{SP}_{0\text{Zn}}$ synthesized without ZnO addition, it exhibited pronounced characteristic peaks belonging to CHA/AEI intergrowth [47]. Fig. S1 displays the comparison of the experimental XRD patterns of the samples with those simulated with DIFFaX, revealing that there is about 30–40 % of AEI phase and 60–70 % of CHA phase in the intergrowth structure of $\text{SP}_{0\text{Zn}}$. This indicates that the introduction of a small amount of ZnO can efficiently inhibit the AEI intergrowth in the product. The compositions of the samples are listed in Table 1. All samples contain a low Si content of about 7 %. The Si contents in $\text{SP}_{0.02\text{Zn}}$ and $\text{SP}_{0\text{Zn}}$ are slightly higher than in their corresponding precursors, implying that the etched part of $\text{SP}_{0.02\text{Zn}}$ -P and $\text{SP}_{0\text{Zn}}$ -P is relatively lack in Si. Moreover, the Zn residue in $\text{SP}_{0.02\text{Zn}}$ is only 0.028 wt%, which is significantly lower than that in its precursor (0.494 wt%), evidencing the effectiveness of the etching process (III stage) for the removal of Zn-containing compositions.

The N_2 adsorption isotherms of the calcined samples are given in Fig. S2, which present a type I isotherm. The micropore volume and micropore surface area of $\text{SP}_{0.02\text{Zn}}$ are 0.28 $\text{cm}^3 \cdot \text{g}^{-1}$ and 585 $\text{m}^2 \cdot \text{g}^{-1}$, respectively, a bit higher than that of reference sample $\text{SP}_{0\text{Zn}}$ (0.26 $\text{cm}^3 \cdot \text{g}^{-1}$ and 572 $\text{m}^2 \cdot \text{g}^{-1}$) (Table S1), confirming the high crystallinity of the synthesized low-silica SAPO-34. SEM images shown in Fig. 2d and e reveal that $\text{SP}_{0.02\text{Zn}}$ has a hollow box morphology with wall thickness of about 100–300 nm. This is distinct from the perfect cubic crystals of $\text{SP}_{0.02\text{Zn}}$ -P precursor (Fig. 2f and g) and agrees with the decrease of solid yield from 85.9 % to 64.1 %, although the crystal phase and relative crystallinity of $\text{SP}_{0.02\text{Zn}}$ are basically unchanged after in situ etching process (Fig. 2a). For the reference samples synthesized without ZnO addition, the crystal morphology seems no apparent change before and

Table 1
Solid yields, product phases and compositions.

Sample	Yield (%) ^[a]	Product phase	Si/(Si + Al + P) in mole ^[b]	Zn content (wt %) ^[b]	Unit cell composition ^[c]
$\text{SP}_{0.02\text{Zn}}$	66.1	CHA	0.070	0.028	[TEA _{3.1} (H ₂ O) _{9.1}] [Si _{2.5} Al _{18.0} P _{15.5} O ₇₂]
$\text{SP}_{0.02\text{Zn}}$ -P	85.9	CHA	0.067	0.494	[TEA _{3.4} (H ₂ O) _{10.4}] [Si _{2.4} Al _{17.9} P _{15.6} Zn _{0.2} O ₇₂]
$\text{SP}_{0\text{Zn}}$	58.8	CHA/ AEI	0.067	0	[TEA _{3.3} (H ₂ O) _{9.9}] [Si _{2.4} Al _{18.3} P _{15.3} O ₇₂]
$\text{SP}_{0\text{Zn}}$ -P	86.1	CHA/ AEI	0.065	0	[TEA _{3.1} (H ₂ O) _{9.0}] [Si _{2.3} Al _{18.0} P _{15.7} O ₇₂]

[a] Yield (%) = ($M_{\text{product}} \times 85 \% / M_{\text{gel}} \times 100$ %), where M_{product} and M_{gel} stand for the weight of the as-synthesized solid products and the dry mass of inorganic oxides in the starting gel, respectively.

[b] Determined by XRF.

[c] Determined by XRF and TG.

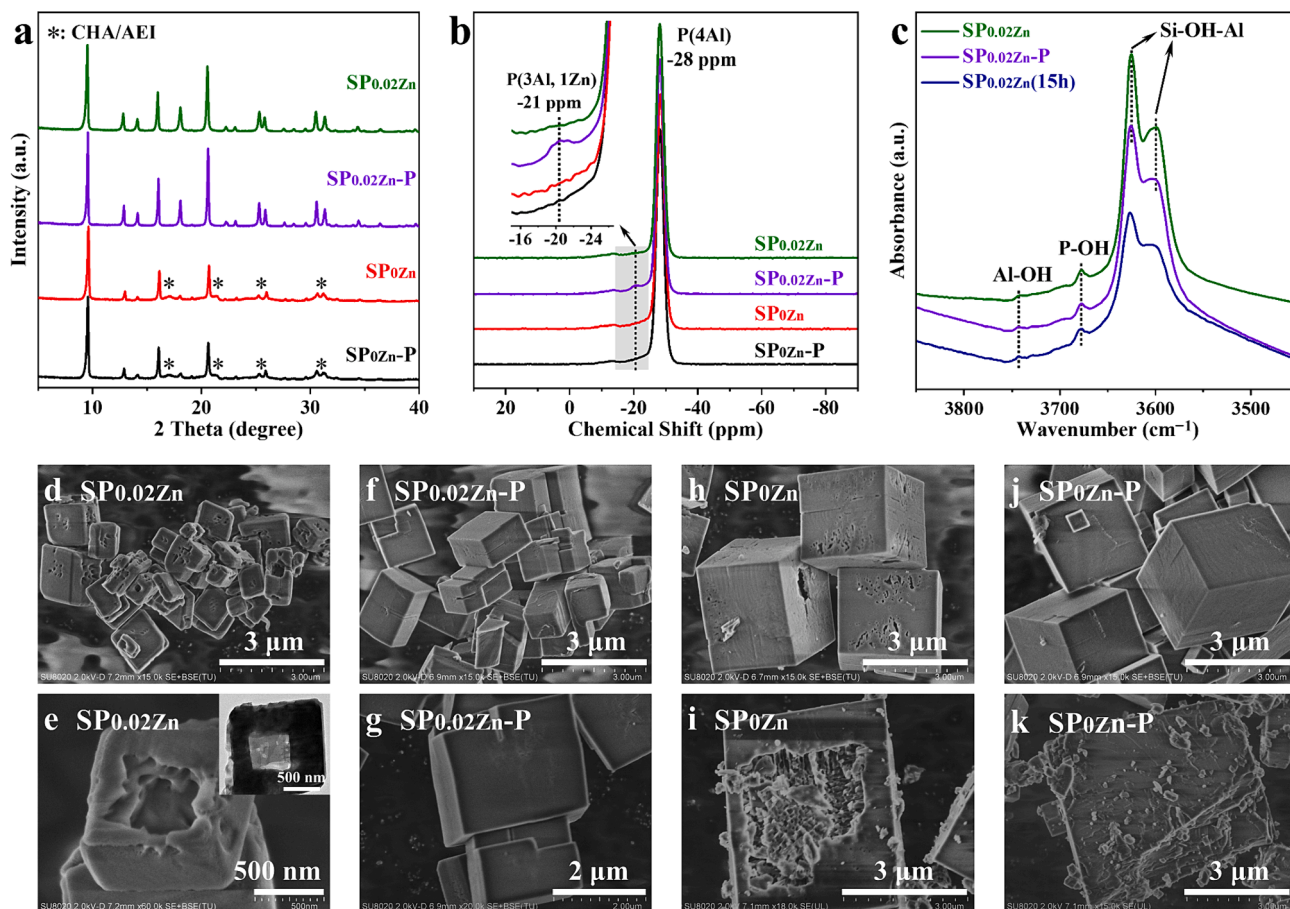


Fig. 2. (a) XRD patterns and (b) ^{31}P MAS NMR spectra of the as-synthesized samples. (c) FTIR spectra of the $\nu(\text{OH})$ vibration region of the calcined samples. (d–k) SEM images of the as-synthesized samples. The inset in (e) is the corresponding TEM image. The (i) and (k) are SEM images of crushed samples to show the inner of the crystals.

after etching process (Fig. 2h and j). However, a further grinding treatment reveals the hollow interior of $\text{SP}_{0\text{Zn}}$ (Fig. 2i and k), which demonstrates that the sample synthesized without ZnO ($\text{SP}_{0\text{Zn-P}}$) also suffered etching in the III stage and led to the reduced product yield. These results suggest that the etching occurs selectively in the crystal interior of the SAPO material, whatever the addition of ZnO or not.

The ^{31}P MAS NMR spectra of the as-synthesized samples (Fig. 2b) show a dominant signal at -28 ppm corresponding to the framework P (4Al) species [48]. Moreover, a weak signal at -21 ppm can be observed in the spectrum of $\text{SP}_{0.02\text{Zn-P}}$. Considering the existence of Zn atoms in $\text{SP}_{0.02\text{Zn-P}}$ (~ 0.5 wt%), it is supposed that the signal may arise from P (3Al, 1Zn) owing to the formation of P-O-Zn bonds [41,42,49]. To confirm this assignment, a series of ZnAPSO-34 with varied Zn contents were synthesized (Fig. S3) and their ^{31}P spectra were measured. From Fig. S4, the signal at -21 ppm gradually accumulates with the increase of Zn content, verifying the assignment well. The formation of P(3Al, 1Zn) species evidences the existence of Zn in the framework of $\text{SP}_{0.02\text{Zn-P}}$. The ^{29}Si MAS NMR spectra of the samples (Fig. S5a) present a dominant peak at -92 ppm exclusively, demonstrating the presence of isolated Si(4Al) species and the absence of silica islands [50]. The ^{27}Al MAS NMR spectra of the samples are displayed in Fig. S5b. The intense peak at 40 ppm arises from tetrahedral Al. The weak peak appearing at 13 ppm should be due to pentacoordinate Al atoms formed by interaction of template or/and water with framework Al atoms [51]. Less pronounced changes in the ^{29}Si and ^{27}Al spectra can be found for $\text{SP}_{0.02\text{Zn}}$ and $\text{SP}_{0\text{Zn}}$ in comparison with their unetched precursors. These results imply that the etching of Zn-containing components during the III stage has little effect on the coordination environments of the

framework atoms.

Fig. 2c shows the $\nu(\text{OH})$ vibration region of the FTIR spectra of the calcined samples. Clearly, $\text{SP}_{0.02\text{Zn-P}}$ and $\text{SP}_{0.02\text{Zn}}$ possess similar spectra with the existence of very small amount of Al-OH and P-OH defects [52]. NH_3 -TPD experiments are carried out to learn the acid properties of the samples. The results are illustrated in Fig. S6 and Table S2. The samples before and after the etching process have almost the same NH_3 -TPD curves and acid amounts.

The MTO reaction results of the samples are summarized in Fig. 3a, 3b and Table 2. Under the investigated conditions, the $\text{SP}_{0.02\text{Zn}}$ exhibited the longest catalytic lifetime of 276 min and the highest ethylene plus propylene selectivity of 86.9 wt%. The results are at the top level even among the low-silica SAPO-34 catalysts (Table S3). It is noted that the trace amount of Zn in $\text{SP}_{0.02\text{Zn}}$ did not cause the extra CH_3OH decomposition (giving CO and CO_2 products). This agrees with our previous works on the Zn-modified SAPO-34, which gave only a trace amount of CO and CO_2 in the MTO reaction [53]. The lifetime of $\text{SP}_{0.02\text{Zn-P}}$ was significantly shortened (157 min) than that of $\text{SP}_{0.02\text{Zn}}$. Given the similar acid amounts of $\text{SP}_{0.02\text{Zn}}$ and $\text{SP}_{0.02\text{Zn-P}}$, the fast deactivation and higher coke deposition rate observed for $\text{SP}_{0.02\text{Zn-P}}$ are supposed to be due to its solid morphology and the existence of Zn (0.494 wt%). The latter (as Lewis acid sites) has been evidenced to prompt the dehydrogenation and cyclization of alkanes/alkenes and thus the formation of aromatics and coke [54–56]. On the other hand, the reference sample $\text{SP}_{0\text{Zn}}$ containing about 30–40 % of SAPO-18 intergrowth shows shorter catalytic lifetime (225 min) than $\text{SP}_{0.02\text{Zn}}$ and obviously low selectivity of ethylene plus propylene (83.2 wt%). This result is reasonable as previous work has demonstrated that the relatively large *aei* cage of SAPO-18 can allow the

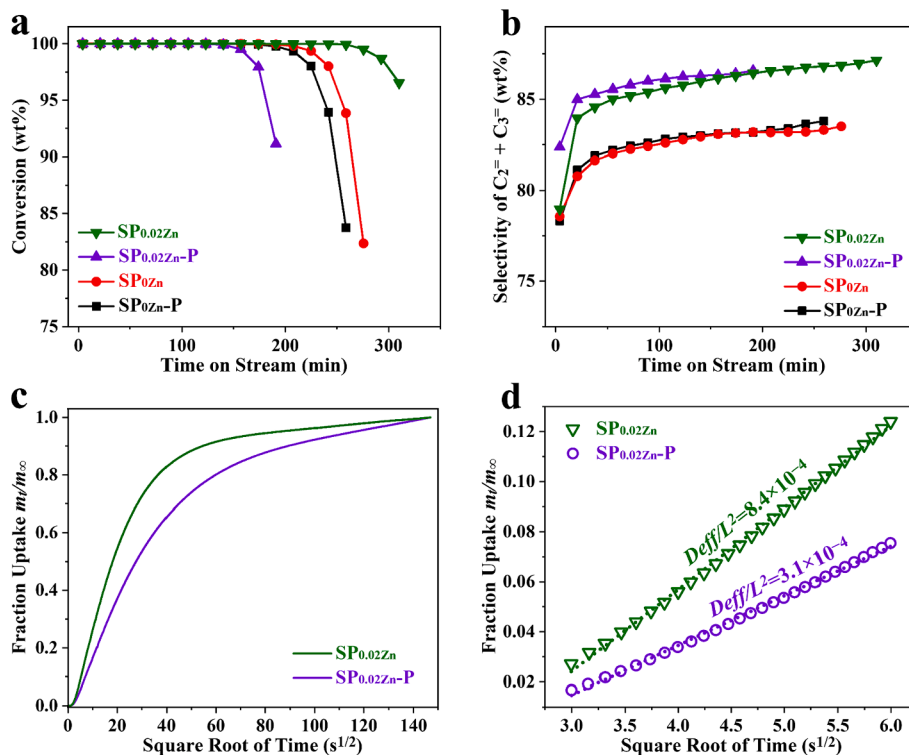


Fig. 3. (a) Methanol conversion and (b) selectivity of ethylene plus propylene with time on stream over samples. Reaction conditions: $\text{WHSV}_{\text{methanol}} = 3.65 \text{ h}^{-1}$, $T = 450 \text{ }^\circ\text{C}$. (c) Propane uptake rate curves of the investigated catalysts. (d) Initial uptake rate. The symbols and dashed lines represent the experimental data and fitting results by eq (2) in the section 2.5, respectively.

Table 2

Lifetime and products distribution of the samples in the MTO reaction.

Sample	Lifetime ^[a] (min)	C ₂ ⁻ (wt%)	C ₃ ⁻ (wt%)	C ₂ ⁻ +C ₃ ⁻ [b] (wt%)	Coke content ^[c] (% g g ⁻¹ cat)	R _{coke} ^[c] (mg g ⁻¹ cat min ⁻¹)	D _{eff} /L ² (s ⁻¹)
SP _{0.02Zn}	276	55.0	31.9	86.9	27.3	0.88	8.4 × 10 ⁻⁴
SP _{0.02Zn-P}	157	55.0	31.3	86.3	24.1	1.21	3.1 × 10 ⁻⁴
SP _{0Zn}	225	48.3	34.9	83.2	25.9	0.91	7.1 × 10 ⁻⁴
SP _{0Zn-P}	208	49.0	34.3	83.3	25.9	1.07	2.5 × 10 ⁻⁴

[a] Reaction conditions: $\text{WHSV}_{\text{methanol}} = 3.65 \text{ h}^{-1}$, $T = 450 \text{ }^\circ\text{C}$. Catalyst lifetime is defined as the reaction duration with >99 % methanol conversion.

[b] The highest selectivity of C₂⁻ and C₃⁻ under >99 % methanol conversion.

[c] Determined based on the weight loss between 200–900 °C in the TG curves of the spent catalysts. $R_{\text{coke}} = \text{coke amount}/(\text{catalyst weight} * \text{reaction time})$.

formation of larger active polyaromatic intermediates, leading to the decrease of ethylene selectivity, but the increase of propylene and butylene [4]. This also emphasizes the importance of pure CHA phase for achieving high selectivity of ethylene plus propylene. The catalytic lifetime of SP_{0Zn-P} was shorter than SP_{0Zn}, similar as those observed for SP_{0.02Zn}/SP_{0.02Zn-P}, which implies the improved mass transfer properties in the hollow catalysts. The coking rates are also displayed in Table 2, which show good consistence with the catalytic lifetimes of the samples.

The transport properties of the catalysts were further evaluated by IGA. As shown in Fig. 3c, the propane uptake rate on hollow SP_{0.02Zn} is obviously faster than on SP_{0.02Zn-P}. Quantitative analyses were carried out based on Fick's second law (Eq. (2)). The fitting results of m_t/m_∞ versus $t^{1/2}$ show a good linearity (Fig. 3d), and the diffusion time constant (D_{eff}/L^2), good indicators of the mass transfer properties, could be evaluated from the slopes [45,46,57]. The calculated D_{eff}/L^2 value is 8.4×10^{-4} for SP_{0.02Zn} and 3.1×10^{-4} for SP_{0.02Zn-P}, evidencing the better mass transfer properties of SP_{0.02Zn}. The IGA results of SP_{0Zn} and SP_{0Zn-P} evidence that the hollow SP_{0Zn} also shows better mass transfer properties than the latter (Fig. S7).

3.2. Effect of crystallization conditions on synthesis

To elucidate the crucial parameters for the formation of the hollow low-silica SAPO-34, syntheses with varied SiO₂ and ZnO addition in the initial gel were investigated. As shown in Table S4 and Fig. S8, sufficient SiO₂ addition was important for a successful synthesis. When the SiO₂ dosage dropped to 0.20, the yield decreased and the products became a mixture of CHA and AFI phases. However, the appearance of tiny amount of ZnO was found to be effective for restraining the intergrowth of CHA/AEI. Product with apparent CHA phase can be obtained when the ZnO dosage was as low as 0.01.

The importance of the crystallization at 160 °C (the I stage) for the synthesis is illustrated in Fig. 4 and Table S5. A CHA/AEI intergrowth (SP_{0.02Zn}-200) was obtained when the synthesis was carried out without the crystallization at 160 °C. SP_{0.02Zn}-200 possesses a hollow morphology similar as SP_{0.02Zn}. The Zn content of SP_{0.02Zn}-200 is close to its precursor SP_{0.02Zn}-200-P, which is distinct from that observed for SP_{0.02Zn}/SP_{0.02Zn-P} (Table 1). This implies a homogenous Zn distribution in the crystals of SP_{0.02Zn}-200-P, as evidenced by XPS results (Table 3). It is speculated that the increased reactivity of Si source at 200 °C reduces the Zn incorporation degree in SP_{0.02Zn}-200-P, causing

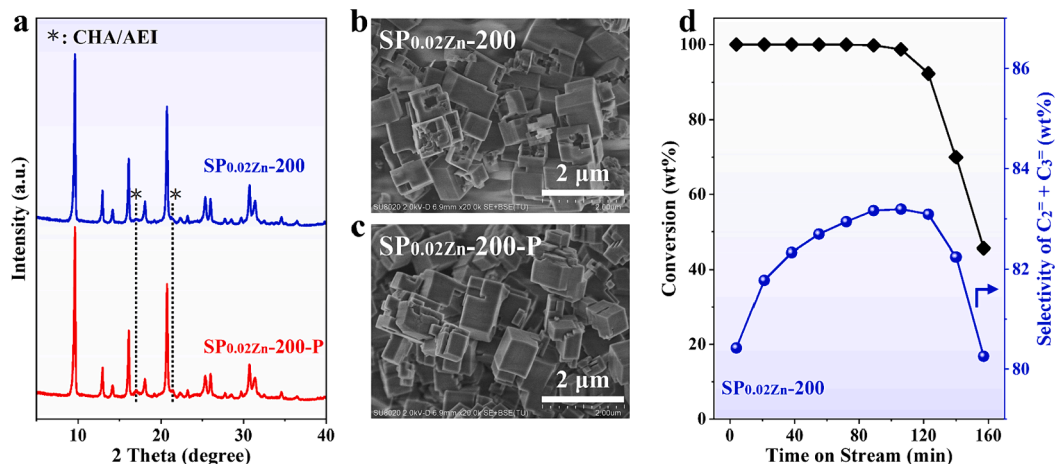


Fig. 4. (a) XRD patterns and (b, c) SEM images of $\text{SP}_{0.02\text{Zn}}\text{-200-P}$ and $\text{SP}_{0.02\text{Zn}}\text{-200}$ synthesized without the low-temperature (I) crystallization stage. (d) Methanol conversion and selectivity of ethylene plus propylene with time on stream over $\text{SP}_{0.02\text{Zn}}\text{-200}$. Reaction conditions: $\text{WHSV}_{\text{methanol}} = 3.65 \text{ h}^{-1}$, $T = 450 \text{ }^\circ\text{C}$, catalyst weight = 300 mg.

Table 3

Bulk and surface compositions of the samples.

Sample	Bulk composition (XRF)		Surface composition (XPS)
	Normalization to TO_2 (in mole)	Zn content (wt%)	Normalization to TO_2 (in mole)
$\text{SP}_{0.02\text{Zn}}$ (10 h)	$\text{Al}_{0.489}\text{Si}_{0.057}\text{P}_{0.439}\text{Zn}_{0.015}\text{O}_2$	1.648	$\text{Al}_{0.471}\text{Si}_{0.080}\text{P}_{0.431}\text{Zn}_{0.017}\text{O}_2$
$\text{SP}_{0.02\text{Zn}}$ (15 h)	$\text{Al}_{0.492}\text{Si}_{0.063}\text{P}_{0.436}\text{Zn}_{0.009}\text{O}_2$	0.924	$\text{Al}_{0.472}\text{Si}_{0.082}\text{P}_{0.434}\text{Zn}_{0.012}\text{O}_2$
$\text{SP}_{0.02\text{Zn}}\text{-P}$	$\text{Al}_{0.496}\text{Si}_{0.067}\text{P}_{0.433}\text{Zn}_{0.005}\text{O}_2$	0.494	$\text{Al}_{0.488}\text{Si}_{0.089}\text{P}_{0.423}\text{O}_2$
$\text{SP}_{0.02\text{Zn}}$	$\text{Al}_{0.498}\text{Si}_{0.070}\text{P}_{0.431}\text{O}_2$	0.028	$\text{Al}_{0.503}\text{Si}_{0.101}\text{P}_{0.396}\text{O}_2$
$\text{SP}_{0\text{Zn}}\text{-P}$	$\text{Al}_{0.499}\text{Si}_{0.065}\text{P}_{0.436}\text{O}_2$	0	$\text{Al}_{0.497}\text{Si}_{0.093}\text{P}_{0.409}\text{O}_2$
$\text{SP}_{0\text{Zn}}$	$\text{Al}_{0.508}\text{Si}_{0.067}\text{P}_{0.426}\text{O}_2$	0	$\text{Al}_{0.493}\text{Si}_{0.105}\text{P}_{0.402}\text{O}_2$
$\text{SP}_{0.02\text{Zn}}\text{-200-P}$	$\text{Al}_{0.486}\text{Si}_{0.063}\text{P}_{0.446}\text{Zn}_{0.005}\text{O}_2$	0.576	$\text{Al}_{0.444}\text{Si}_{0.154}\text{P}_{0.380}\text{Zn}_{0.023}\text{O}_2$
$\text{SP}_{0.02\text{Zn}}\text{-200}$	$\text{Al}_{0.489}\text{Si}_{0.066}\text{P}_{0.442}\text{Zn}_{0.004}\text{O}_2$	0.414	$\text{Al}_{0.468}\text{Si}_{0.182}\text{P}_{0.335}\text{Zn}_{0.015}\text{O}_2$

homogenous Zn distribution and restraining its positive effect for inducing pure CHA phase. Fig. 4d shows the inferior MTO catalytic performance of $\text{SP}_{0.02\text{Zn}}\text{-200}$. The importance of seed addition on the synthesis is shown in Fig. S9. The absence of seed in the gel led to a product with large crystal size and higher Zn content. It is speculated that the positive effect of Zn was reduced under conditions with slower nucleation process, causing diminished Zn accumulation in the core of crystals. Moreover, it is noted that the III stage is important for the formation of box morphology, as no etching occurs just by prolonging the crystallization at $200 \text{ }^\circ\text{C}$ for even 20 h.

3.3. Crystallization process investigation

The crystallization process of low-silica $\text{SP}_{0.02\text{Zn}}$ was monitored to figure out the formation mechanism of hollow morphology and to understand how Zn atom plays its role for achieving the pure CHA phase. As a comparison, the crystallization process of $\text{SP}_{0\text{Zn}}$ without the addition of ZnO was also investigated. From the XRD patterns shown in Fig. S10, all the samples of the $\text{SP}_{0.02\text{Zn}}$ system possess pure CHA phase, while those of the $\text{SP}_{0\text{Zn}}$ system exhibit obvious CHA/AEI intergrowth throughout the whole crystallization process, showing that Zn atoms work since the very initial stage. Fig. 5a displays the evolution of solid yields of the samples. In the first stage of crystallization at $160 \text{ }^\circ\text{C}$, the solid yields of the $\text{SP}_{0.02\text{Zn}}$ system are clearly higher than those of the $\text{SP}_{0\text{Zn}}$ system. The yield shows a rapid increase with the crystallization temperature rising to $200 \text{ }^\circ\text{C}$. The two systems show similar and high yields in the II crystallization stage and the values are less changed. In the following III stage, both the yields show a fast drop from $\sim 86 \%$ to $\sim 60 \%$ owing to the occurrence of etching in the crystal interior.

The chemical compositions of the samples are shown in Fig. 5b. The contents of Al and P in the initial $\text{SP}_{0.02\text{Zn}}$ (5 h) have almost reached

equilibrium values, which show little change in the following crystallization. On the contrary, the $\text{SP}_{0\text{Zn}}$ (5 h) sample possesses excessive Al content (62.9 %), confirming the existence of amorphous particles observed in the SEM images (Fig. 5e). The product Si contents in both systems present an increasing trend from $\sim 5.0 \%$ to $\sim 7.0 \%$ with the proceeding of crystallization, implying a gradual incorporation of Si into the framework. For the evolution of Zn content of the $\text{SP}_{0.02\text{Zn}}$ system, the initial $\text{SP}_{0.02\text{Zn}}$ (5 h) sample has the highest Zn content of 2.6 wt%, which decreases gradually to $\sim 0.5 \%$ wt% at the end of the II stage and further drops to 0.028 wt% after the III stage (etching). Notably, the utilization of Zn in $\text{SP}_{0.02\text{Zn}}$ (5 h) is obviously higher than that of Si (Fig. 5c, 71.9 % vs 9.8 %), which suggests the relatively high reaction activity of Zn species at the initial crystallization stage ($160 \text{ }^\circ\text{C}$). Moreover, given the gradually increased solid yield of $\text{SP}_{0.02\text{Zn}}$ system before 18 h, the reduced Zn contents in the products suggest that the newly crystallized solids should be SAPO-rich, but Zn-deficient.

The SEM images of the samples are displayed in Fig. 5d and e. Only perfect crystals can be found for the initial $\text{SP}_{0.02\text{Zn}}$ (5 h) sample, while small amount of amorphous particles still exist for $\text{SP}_{0\text{Zn}}$ (10 h). This indicates that ZnO addition can effectively accelerate the nucleation and the subsequent crystallization, as evidenced by the solid yield results (Fig. 5a). The crystal sizes of the two systems increase slowly following the proceeding of crystallization. The sizes of $\text{SP}_{0.02\text{Zn}}$ system are always smaller than those of $\text{SP}_{0\text{Zn}}$ system, which should be owing to the increased nucleation prompted by Zn atoms.

The XPS results of the samples are shown in Table 3. The surface Zn contents of the samples of $\text{SP}_{0.02\text{Zn}}$ system show a decrease trend from $\text{SP}_{0.02\text{Zn}}$ (10 h) to $\text{SP}_{0.02\text{Zn}}\text{-P}$, in agreement with the composition evolution of the bulk phase. Given the absence of Zn species on the surface of $\text{SP}_{0.02\text{Zn}}\text{-P}$ and the almost complete utilization of Zn for $\text{SP}_{0.02\text{Zn}}$ (15 h) (Fig. 5c), it is speculated that the $\text{SP}_{0.02\text{Zn}}\text{-P}$ crystals have a core-shell

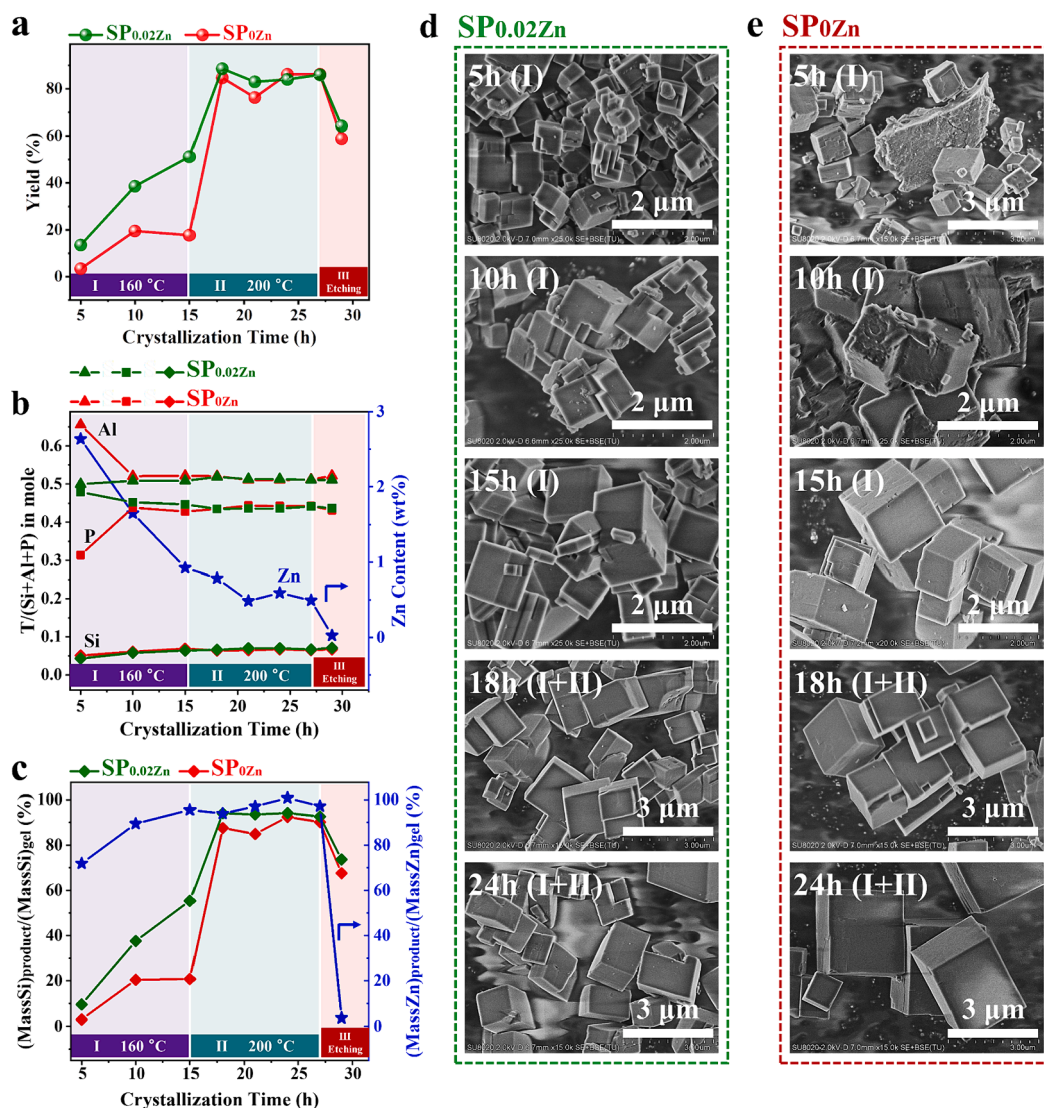


Fig. 5. (a) Solid yields, (b, c) chemical compositions and (d, e) SEM images of the as-synthesized samples following the evolution of crystallization time.

structure (ZnAPSO-34@SAPO-34) with enriched Zn species in the interior of the crystals. Moreover, all samples possess higher surface Si content than the bulk phase, which implies an increased Si content from the core to the shell of the crystals and consists with our previous findings [58].

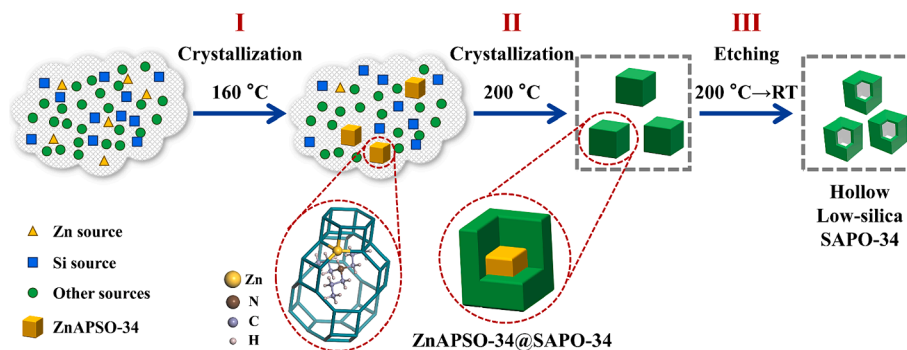
In summary, the Zn atoms take participant in the framework formation of low-silica SAPO-34 since the initial stage at 160 °C, owing to the rapid and facile formation of Zn-O-P bonds (Fig. 2b) [59]. The negative Zn-O-P bonds are supposed to have strong interactions with the protonated TEA cations, and thus help direct the formation of pure CHA phase. Similar findings have also been reported by previous works [42,60]. Owing to the high framework incorporation ability of Zn in the first stage (Fig. 5c), the product crystals (before etching) possess Zn-enriched core and thus a core-shell structure of ZnAPSO-34@SAPO-34. Regarding the formation of hollow morphology, the similar morphology observed for SP_{0.02Zn}, SP_{0Zn}, SP_{0.02Zn}-200 and SP_{0Zn}-200 (Figs. 2, 4 and S11) and the less changed Zn content between SP_{0.02Zn}-200-P and SP_{0.02Zn}-200 (Table 3) suggest that the existence of Zn atoms is not the key factor for inducing the etching of ZnAPSO-34@SAPO-34. It is generally acknowledged that the etching of molecular sieve crystals is guided by defect sites [61–63] and/or inhomogeneous spatial distribution of framework T atoms [64–66]. Herein, given that the ZnAPSO-34 core (sample SP_{0.02Zn}(15 h)) has similar defect amount as that of

ZnAPSO-34@SAPO-34 and the etched product (Fig. 2c), it is speculated that the inhomogeneous P distribution in the crystals may be the main reason for the occurrence of biased etching in alkaline mother liquid, as the [PO₄]⁺ has the worst resistance to the attacks of OH⁻ among the framework TO₄ species [67]. That is, the relatively high P content of the crystal interior (0.439_{bulk} for SP_{0.02Zn}(10 h) vs 0.423_{surface} for SP_{0.02Zn}-P, Table 3) results in the priority etching therein. On the basis of the above discussions, the formation of pure phase low-silica SAPO-34 with hollow morphology are rationalized and illustrated in Scheme 1.

3.4. Synthesis of hollow low-silica SAPO-34 with mother liquid and other metal sources

The present strategy provides a facile and inexpensive route for the preparation of highly efficient SAPO-34 catalyst. To further improve the environmental friendliness of the synthesis, the mother liquid after the synthesis was collected, analyzed and used as partial sources for a renewed synthesis. The details of the synthesis are presented in Fig. S12. Both the composition, crystallinity and morphology of SP_{0.02Zn}-MLRecycle resemble those of SP_{0.02Zn} synthesized with conventional sources. This proves that recycled mother liquid can be reused to synthesize low-silica SAPO-34 with high quality.

In addition to ZnO, more metal sources (Me = Mg, Mn, Ni and Co)



Scheme 1. Proposed formation mechanism of hollow low-silica SAPO-34 by Zn assistance and in situ etching strategy.

were explored for the synthesis of low-silica SAPO-34, as they have exhibited better incorporation ability into the SAPO framework [68–70]. As displayed in Fig. S13, the XRD patterns of the samples evidence the good ability of these metals for inducing the formation of pure CHA phase. The corresponding SEM images show that the products are hollow cubic morphology. The product compositions are shown in Table S6. It can be seen that Mg is easily removed from the framework, yielding hollow SAPO-34 with a Si content of ~ 0.07 . The residue masses of Mn and Co in the final products are slightly higher than that of $SP_{0.02Zn}$. However, for the Ni-containing synthesis, the Ni contents in the products before and after etching only show little change, which implies the relatively homogenous distribution of Ni atoms in the crystals. The MTO catalytic performance of these samples are displayed in Fig. S14 and Table S7. $SP_{0.02Mg}$ presents long catalytic lifetime (293 min) together with high selectivity of ethylene plus propylene (maximum of 86.6 wt%). The values are comparable with those of $SP_{0.02Zn}$. The other three samples also exhibit better catalytic performance than reference sample SP_{0Zn} . Characterizations (Fig. S15, Table S1 and S2) show that both the mass transfer properties and acidity of $SP_{0.02Mg}$ are comparable with those of $SP_{0.02Zn}$, which should contribute to its excellent MTO catalyst performance.

4. Conclusions

In summary, a metal assistance and in situ etching strategy was developed to synthesize hollow low-silica SAPO-34 (wall thickness of 100–300 nm) by using low-cost TEA template. The simultaneous achievement of pure CHA phase, suitable acidity and good mass transfer property helps the material exhibit excellent MTO catalytic performance with long lifespan and high ethylene plus propylene selectivity. Based on Zn-containing low-silica gel, it was revealed that Zn atoms were more active than Si to participate in the nucleation of ZnAPSO-34, which effectively inhibited the CHA/AEI intergrowth. ZnAPSO-34@SAPO-34 was obtained with further crystallization, which was followed by selective etching of Zn-containing components in subsequent cooling stage. The relatively high P content ($[PO_4]^+$ species) in the crystal interior, which is more susceptible to the alkaline mother liquid, is speculated to cause the priority etching therein. Moreover, mother liquid of synthesis can be recycled for the synthesis of target product. It is believed that this facile strategy offers an attractive alternative for preparing highly efficient MTO catalyst. We hope that the discoveries in this work provide more ideas for exploring the synergic control of SAPO synthesis.

CRediT authorship contribution statement

Xiaosi Zhang: Writing – original draft, Validation, Investigation, Formal analysis, Data curation. **Miao Yang:** Writing – review & editing, Visualization, Validation, Funding acquisition, Conceptualization. **Dong Fan:** Writing – review & editing, Funding acquisition, Formal analysis.

Ye Wang: Formal analysis. **Caiyi Lou:** Formal analysis. **Haocheng Hu:** Formal analysis. **Bing Li:** Funding acquisition. **Peng Tian:** Visualization, Supervision, Funding acquisition, Validation. **Zhongmin Liu:** Visualization, Supervision, Funding acquisition, Validation.

Declaration of competing interest

The authors declare that they have no known competing financial interests or personal relationships that could have appeared to influence the work reported in this paper.

Data availability

Data will be made available on request.

Acknowledgements

The authors gratefully acknowledge the National Natural Science Foundation of China (No. 22288101, 21991090, 21991091, 22171259, 22272173), the AI S&T Program of Yulin Branch, Dalian National Laboratory For Clean Energy, Chinese Academy of Sciences (No. DNL-YL A202206) and DICP funding (DICP 1202420).

Appendix A. Supplementary data

Supplementary data to this article can be found online at <https://doi.org/10.1016/j.cej.2024.151101>.

References

- [1] M.E. Davis, Ordered porous materials for emerging applications, *Nature* 417 (6891) (2002) 813–821, <https://doi.org/10.1038/nature00785>.
- [2] V. Valtchev, L. Tosheva, Porous nanosized particles: preparation, properties, and applications, *Chem. Rev.* 113 (8) (2013) 6734–6760, <https://doi.org/10.1021/cr300439k>.
- [3] Y. Li, J.H. Yu, Emerging applications of zeolites in catalysis, separation and host-guest assembly, *Nat. Rev. Mater.* 6 (12) (2021) 1156–1174, <https://doi.org/10.1038/s41578-021-00347-3>.
- [4] J.R. Chen, J.Z. Li, Y.X. Wei, C.Y. Yuan, B. Li, S.T. Xu, Y. Zhou, J.B. Wang, M. Z. Zhang, Z.M. Liu, Spatial confinement effects of cage-type SAPO molecular sieves on product distribution and coke formation in methanol-to-olefin reaction, *Catal. Commun.* 46 (2014) 36–40, <https://doi.org/10.1016/j.catcom.2013.11.016>.
- [5] I. Pinilla-Herrero, U. Olsbye, C. Márquez-Álvarez, E. Sastre, Effect of framework topology of SAPO catalysts on selectivity and deactivation profile in the methanol-to-olefins reaction, *J. Catal.* 352 (2017) 191–207, <https://doi.org/10.1016/j.jcat.2017.05.008>.
- [6] M. Yang, B. Li, M.B. Gao, S.F. Lin, Y. Wang, S.T. Xu, X.B. Zhao, P. Guo, Y.X. Wei, M. Ye, P. Tian, Z.M. Liu, High propylene selectivity in methanol conversion over a small pore SAPO molecular sieve with ultra-small cage, *ACS Catal.* 10 (6) (2020) 3741–3749, <https://doi.org/10.1021/acscatal.9b04703>.
- [7] W. Dai, X. Wang, G. Wu, N. Guan, M. Hunger, L. Li, Methanol-to-olefin conversion on silicoaluminophosphate catalysts: effect of bronsted acid sites and framework structures, *ACS Catal.* 1 (4) (2011) 292–299, <https://doi.org/10.1021/cs200016u>.
- [8] B. Gao, M. Yang, Y. Qiao, J. Li, X. Xiang, P. Wu, Y. Wei, S. Xu, P. Tian, Z. Liu, A low-temperature approach to synthesize low-silica SAPO-34 nanocrystals and their application in the methanol-to-olefins (MTO) reaction, *Catal. Sci. Technol.* 6 (20) (2016) 7569–7578, <https://doi.org/10.1039/c6cy01461e>.

- [9] D. Chen, K. Moljord, T. Fuglerud, A. Holmen, The effect of crystal size of SAPO-34 on the selectivity and deactivation of the MTO reaction, *Microporous Mesoporous Mater.* 29 (1) (1999) 191–203, [https://doi.org/10.1016/S1387-1811\(98\)00331-X](https://doi.org/10.1016/S1387-1811(98)00331-X).
- [10] Y. Wang, J.F. Han, N. Wang, B. Li, M. Yang, Y.M. Wu, Z.X. Jiang, Y.X. Wei, P. Tian, Z.M. Liu, Conversion of methanol to propylene over SAPO-14: Reaction mechanism and deactivation, *Chin. J. Catal.* 43 (8) (2022) 2259–2269, [https://doi.org/10.1016/S1872-2067\(22\)64123-8](https://doi.org/10.1016/S1872-2067(22)64123-8).
- [11] D.P. Serrano, J.M. Escola, P. Pizarro, Synthesis strategies in the search for hierarchical zeolites, *Chem. Soc. Rev.* 42 (9) (2013) 4004–4035, <https://doi.org/10.1039/C2CS35330J>.
- [12] J. Kim, C. Jo, S. Lee, R. Ryoo, Bulk crystal seeding in the generation of mesopores by organosilane surfactants in zeolite synthesis, *J. Mater. Chem. A* 2 (30) (2014) 11905–11912, <https://doi.org/10.1039/C4TA01948B>.
- [13] C. Wang, M. Yang, P. Tian, S.T. Xu, Y. Yang, D.H. Wang, Y.Y. Yuan, Z.M. Liu, Dual template-directed synthesis of SAPO-34 nanosheet assemblies with improved stability in the methanol to olefins reaction, *J. Mater. Chem. A* 3 (10) (2015) 5608–5616, <https://doi.org/10.1039/c4ta06124a>.
- [14] Database of Zeolite Structures, Framework Type **CHA**. <https://asia.iza-structure.org/IZA-SC/framework.php?STC=CHA>. (Accessed 18 March 2024).
- [15] M. Yang, D. Fan, Y. Wei, P. Tian, Z. Liu, Recent progress in methanol-to-olefins (MTO) catalysts, *Adv. Mater.* 31 (50) (2019) 1902181, <https://doi.org/10.1002/adma.201902181>.
- [16] N. Wang, L. Wang, Y.C. Zhi, J.F. Han, C.W. Zhang, X.Q. Wu, J.L. Zhang, L.Y. Wang, B.H. Fan, S.T. Xu, Y.J. Zheng, S.F. Lin, R.N. Wu, Y.X. Wei, Z.M. Liu, Coking and decoking chemistry for resource utilization of polycyclic aromatic hydrocarbons (PAHs) and low-carbon process, *J. Energy Chem.* 76 (2023) 105–116, <https://doi.org/10.1016/j.jechem.2022.09.014>.
- [17] S. Lin, Y. Zhi, W. Zhang, X. Yuan, C. Zhang, M. Ye, S. Xu, Y. Wei, Z. Liu, Hydrogen transfer reaction contributes to the dynamic evolution of zeolite-catalyzed methanol and dimethyl ether conversions: Insight into formaldehyde, *Chin. J. Catal.* 46 (2023) 11–27, [https://doi.org/10.1016/S1872-2067\(22\)64194-9](https://doi.org/10.1016/S1872-2067(22)64194-9).
- [18] Y. Ni, Y. Liu, Z. Chen, M. Yang, H. Liu, Y. He, Y. Fu, W. Zhu, Z. Liu, Realizing and recognizing syngas-to-olefins reaction via a dual-bed catalyst, *ACS Catal.* 9 (2) (2019) 1026–1032, <https://doi.org/10.1021/acscatal.8b04794>.
- [19] X. Liu, M. Wang, H. Yin, J. Hu, K. Cheng, J. Kang, Q. Zhang, Y. Wang, Tandem catalysis for hydrogenation of CO and CO₂ to lower olefins with bifunctional catalysts composed of spinel oxide and SAPO-34, *ACS Catal.* 10 (15) (2020) 8303–8314, <https://doi.org/10.1021/acscatal.0c01579>.
- [20] Z.P. Liu, Y.M. Ni, Z.P. Hu, Y. Fu, X.D. Fang, Q.K. Jiang, Z.Y. Chen, W.L. Zhu, Z. M. Liu, Insights into effects of ZrO₂ crystal phase on syngas-to-olefin conversion over ZnO/ZrO₂ and SAPO-34 composite catalysts, *Chin. J. Catal.* 43 (3) (2022) 877–884, [https://doi.org/10.1016/S1872-2067\(21\)63908-6](https://doi.org/10.1016/S1872-2067(21)63908-6).
- [21] F. Gao, E.D. Walter, N.M. Washton, J. Szanyi, C.H.F. Peden, Synthesis and evaluation of Cu-SAPO-34 catalysts for ammonia selective catalytic reduction. 1. Aqueous solution ion exchange, *ACS Catal.* 3(9) (2013) 2083–2093. doi: 10.1021/cs4004672.
- [22] X. Xiang, M. Yang, B. Gao, Y. Qiao, P. Tian, S. Xu, Z. Liu, Direct Cu²⁺ ion-exchanged into as-synthesized SAPO-34 and its catalytic application in the selective catalytic reduction of NO with NH₃, *RSC Adv.* 6 (15) (2016) 12544–12552, <https://doi.org/10.1039/C5RA22868A>.
- [23] J. Wang, H. Zhao, G. Haller, Y. Li, Recent advances in the selective catalytic reduction of NO_x with NH₃ on Cu-Chabazite catalysts, *Appl. Catal., B* 202 (2017) 346–354, <https://doi.org/10.1016/j.apcatb.2016.09.024>.
- [24] Q.M. Sun, Z.K. Xie, J.H. Yu, The state-of-the-art synthetic strategies for SAPO-34 zeolite catalysts in methanol-to-olefin conversion, *Natl. Sci. Rev.* 5 (4) (2018) 542–558, <https://doi.org/10.1093/nsr/nwx103>.
- [25] S.H. Jung, J.S. Chang, J.S. Hwang, S.E. Park, Selective formation of SAPO-5 and SAPO-34 molecular sieves with microwave irradiation and hydrothermal heating, *Microporous Mesoporous Mater.* 64 (1–3) (2003) 33–39, [https://doi.org/10.1016/S1387-1811\(03\)00501-8](https://doi.org/10.1016/S1387-1811(03)00501-8).
- [26] P. Wang, A. Lv, J. Hu, J.A. Xu, G. Lu, The synthesis of SAPO-34 with mixed template and its catalytic performance for methanol to olefins reaction, *Microporous Mesoporous Mater.* 152 (2012) 178–184, <https://doi.org/10.1016/j.micromeso.2011.11.037>.
- [27] D. Fan, P. Tian, S.T. Xu, D.H. Wang, Y. Yang, J.Z. Li, Q.Y. Wang, M. Yang, Z.M. Liu, SAPO-34 templated by dipropylamine and diisopropylamine: synthesis and catalytic performance in the methanol to olefin (MTO) reaction, *New J. Chem.* 40 (5) (2016) 4236–4244, <https://doi.org/10.1039/c5nj02351c>.
- [28] L. Xu, A.P. Du, Y.X. Wei, Y.L. Wang, Z.X. Yu, Y.L. He, X.Z. Zhang, Z.M. Liu, Synthesis of SAPO-34 with only Si(4Al) species: Effect of Si contents on Si incorporation mechanism and Si coordination environment of SAPO-34, *Microporous Mesoporous Mater.* 115 (3) (2008) 332–337, <https://doi.org/10.1016/j.micromeso.2008.02.001>.
- [29] R. Smith, W. Slawinski, A. Lind, D. Wragg, J. Cavka, B. Arstad, H. Fjellvag, M. Attfield, D. Akporiaye, M. Anderson, Nanoporous intergrowths: how crystal growth dictates phase composition and hierarchical structure in the **CHA/AEI** system, *Chem. Mater.* 27 (12) (2015) 4205–4215, <https://doi.org/10.1021/cm504284x>.
- [30] B. Shen, X. Chen, X. Fan, H. Xiong, H. Wang, W. Qian, Y. Wang, F. Wei, Resolving atomic SAPO-34/18 intergrowth architectures for methanol conversion by identifying light atoms and bonds, *Nat. Commun.* 12 (1) (2021) 2212, <https://doi.org/10.1038/s41467-021-22438-z>.
- [31] O. Vistad, D. Akporiaye, F. Taulelle, K. Lillerud, In situ NMR of SAPO-34 crystallization, *Chem. Mater.* 15 (8) (2003) 1639–1649, <https://doi.org/10.1021/cm021317w>.
- [32] Z. Yan, B. Chen, Y. Huang, A solid-state NMR study of the formation of molecular sieve SAPO-34, *Solid State Nucl. Magn. Reson.* 35 (2) (2009) 49–60, <https://doi.org/10.1016/j.snmr.2008.12.006>.
- [33] L. Zhang, Y. Bates, D. Chen, H. Nie, Y. Huang, Investigations of formation of molecular sieve SAPO-34, *J. Phys. Chem. C* 115 (45) (2011) 22309–22319, <https://doi.org/10.1021/jp208560t>.
- [34] L. Zhang, Y. Huang, Crystallization and catalytic properties of molecular sieve SAPO-34 by a vapor-phase transport method, *J. Mater. Chem. A* 3 (8) (2015) 4522–4529, <https://doi.org/10.1039/c4ta06775d>.
- [35] S. Ahn, H. Lee, S. Hong, Crystallization mechanism of cage-based, small-pore molecular sieves: A case study of **CHA** and **LEV** structures, *Chem. Mater.* 29 (13) (2017) 5583–5590, <https://doi.org/10.1021/acs.chemmater.7b00980>.
- [36] D. Yuan, A. Xing, P. Miao, Q. Sun, L. Cui, H. Wang, L. Ma, F. Chiang, J. Kong, Assembly of sub-crystals on the macroscale and construction of composite building units on the microscale for SAPO-34, *Chem. - Asian J.* 13 (20) (2018) 3063–3072, <https://doi.org/10.1002/asia.201801069>.
- [37] X.S. Zhang, M. Yang, L. Wang, J.F. Han, C.Y. Lou, S.T. Xu, Y.Y. Zhang, R.A. Wu, P. Tian, Z.M. Liu, Recognizing the minimum structural units driving the crystallization of SAPO-34 in a top-down process, *Chem.-Eur. J.* (2023), <https://doi.org/10.1002/chem.202203886>.
- [38] X.S. Zhang, M. Yang, Y. Wang, C.Y. Lou, S.T. Xu, P. Tian, Z.M. Liu, Insights on the seed selection criteria of SAPO-34 synthesis: structural units and their chemical microenvironment, *Inorg. Chem. Front.* 10 (13) (2023) 3874–3883, <https://doi.org/10.1039/d3qi00646h>.
- [39] N.N. Tusar, V. Kaucic, A zinc-rich **CHA**-type aluminophosphate, *Zeolites* 15 (8) (1995) 708–713, [https://doi.org/10.1016/0144-2449\(95\)00046-9](https://doi.org/10.1016/0144-2449(95)00046-9).
- [40] S. Ashtekar, S.V.V. Chilukuri, A.M. Prakash, C.S. Harendranath, D.K. Chakrabarty, Small pore aluminophosphate molecular sieves with chabazite structure: incorporation of cobalt in the structures -34 and -44, *J. Phys. Chem.* 99 (18) (1995) 6937–6943, <https://doi.org/10.1021/j100018a027>.
- [41] F. Deng, Y. Yue, T.C. Xiao, Y.U. Du, C.H. Ye, L.D. An, H.L. Wang, Substitution of aluminum in aluminophosphate molecular-sieve by magnesium-A combined NMR and XRD study, *J. Phys. Chem.* 99 (16) (1995) 6029–6035, <https://doi.org/10.1021/j100016a045>.
- [42] A.M. Beale, M.G. O'Brien, M. Kasunic, A. Golobic, M. Sanchez-Sanchez, A.J. W. Lobo, D.W. Lewis, D.S. Wragg, S. Nikitenko, W. Bras, B.M. Weckhuysen, Probing ZnAPO-34 self-assembly using simultaneous multiple in situ techniques, *J. Phys. Chem. C* 115 (14) (2011) 6331–6340, <https://doi.org/10.1021/jp200043b>.
- [43] M. Yang, P. Tian, C. Wang, Y. Yuan, Y. Yang, S. Xu, Y. He, Z. Liu, A top-down approach to prepare silicoaluminophosphate molecular sieve nanocrystals with improved catalytic activity, *Chem. Commun.* 50 (15) (2014) 1845–1847, <https://doi.org/10.1039/c3cc48264b>.
- [44] M.Y. Kim, K. Lee, M. Choi, Cooperative effects of secondary mesoporosity and acid site location in Pt/SAPO-11 on n-dodecane hydroisomerization selectivity, *J. Catal.* 319 (2014) 232–238, <https://doi.org/10.1016/j.jcat.2014.09.001>.
- [45] D. Jin, G. Ye, J. Zheng, W. Yang, K. Zhu, M.-O. Coppens, X. Zhou, Hierarchical silicoaluminophosphate catalysts with enhanced hydroisomerization selectivity by directing the orientated assembly of premanufactured building blocks, *ACS Catal.* 7 (9) (2017) 5887–5902, <https://doi.org/10.1021/acscatal.7b01646>.
- [46] T. Yue, W. Liu, L. Li, X. Zhao, K. Zhu, X. Zhou, W. Yang, Crystallization of ATO silicoaluminophosphates nanocrystalline spheroids using a phase-transfer synthetic strategy for n-heptane hydroisomerization, *J. Catal.* 364 (2018) 308–327, <https://doi.org/10.1016/j.jcat.2018.06.003>.
- [47] E. Bello-Jurado, D. Schwalbe-Koda, M. Nero, C. Paris, T. Uusimäki, Y. Roman-Leshkov, A. Corma, T. Willhammar, R. Gomez-Bombarelli, M. Moliner, Tunable **CHA/AEI** zeolite intergrowths with a priori biselective organic structure-directing agents: controlling enrichment and implications for selective catalytic reduction of NO_x, *Angew. Chem. Int. Ed.* 61 (28) (2022), <https://doi.org/10.1002/anie.202201837>.
- [48] Y. Huang, D. Machado, C.W. Kirby, A study of the formation of molecular sieve SAPO-44, *J. Phys. Chem. B* 108 (6) (2004) 1855–1865, <https://doi.org/10.1021/jp0308256>.
- [49] T. Blasco, L. Fernandez, A. Martinez-Arias, M. Sanchez-Sanchez, P. Concepcion, J. Nieto, Magnetic resonance studies on V-containing, and V, Mg-containing AFI aluminophosphates, *Microporous Mesoporous Mater.* 39 (1–2) (2000) 219–228, [https://doi.org/10.1016/S1387-1811\(00\)00199-2](https://doi.org/10.1016/S1387-1811(00)00199-2).
- [50] S. Ashtekar, S.V.V. Chilukuri, D.K. Chakrabarty, Small-pore molecular sieves SAPO-34 and SAPO-44 with chabazite structure: A study of siliceous incorporation, *J. Phys. Chem.* 98 (18) (1994) 4878–4883, <https://doi.org/10.1021/j100069a018>.
- [51] C.S. Blackwell, R.L. Patton, Solid-state NMR of silicoaluminophosphate molecular sieves and aluminophosphate materials, *J. Phys. Chem.* 92 (13) (1988) 3965–3970, <https://doi.org/10.1021/j100324a055>.
- [52] S. Bordiga, L. Regli, D. Cocina, C. Lamberti, M. Bjorn, K.P. Lillerud, Assessing the acidity of high silica chabazite H-SSZ-13 by FTIR using CO as molecular probe: comparison with H-SAPO-34, *J. Phys. Chem. B* 109 (7) (2005) 2779–2784, <https://doi.org/10.1021/jp045498w>.
- [53] J.W. Zhong, J.F. Han, Y.X. Wei, S.T. Xu, Y.L. He, Y.J. Zheng, M. Ye, X.W. Guo, C. S. Song, Z.M. Liu, Increasing the selectivity to ethylene in the MTO reaction by enhancing diffusion limitation in the shell layer of SAPO-34 catalyst, *Chem. Commun.* 54 (25) (2018) 3146–3149, <https://doi.org/10.1039/c7cc09239c>.
- [54] S. Muller, Y. Liu, F.M. Kirchberger, M. Tonigold, M. Sanchez-Sanchez, J.A. Lercher, Hydrogen transfer pathways during zeolite catalyzed methanol conversion to hydrocarbons, *J. Am. Chem. Soc.* 138 (49) (2016) 15994–16003, <https://doi.org/10.1021/jacs.6b09605>.

- [55] A. Hagen, F. Roessner, Ethane to aromatic hydrocarbons: past, present, future, *Catal. Rev.-Sci. Eng.* 42 (4) (2000) 403–437, <https://doi.org/10.1081/CR-100101952>.
- [56] M.V. Luzgin, V.A. Rogov, S.S. Arzumanov, A.V. Toktarev, A.G. Stepanov, V. N. Parmon, Understanding methane aromatization on a Zn-modified high-silica zeolite, *Angew. Chem. Int. Ed.* 47 (24) (2008) 4559–4562, <https://doi.org/10.1002/anie.200800317>.
- [57] P. Wu, M. Yang, L. Sun, S. Zeng, S. Xu, P. Tian, Z. Liu, Synthesis of nanosized SAPO-34 with the assistance of bifunctional amine and seeds, *Chem. Commun.* 54 (79) (2018) 11160–11163, <https://doi.org/10.1039/c8cc05871g>.
- [58] P. Tian, B. Li, S.T. Xu, X. Su, D.H. Wang, L. Zhang, D. Fan, Y. Qi, Z.M. Liu, Investigation of the Crystallization Process of SAPO-35 and Si Distribution in the Crystals, *J. Phys. Chem. C* 117 (8) (2013) 4048–4056, <https://doi.org/10.1021/jp311334q>.
- [59] M. Sanchez-Sanchez, D.P. Serrano, R. vanGrieken, J.A. Melero, Nearly room-temperature crystallisation of Zn-doped AlPO_4 -based chabazite materials, in: R. Xu, Z. Gao, J. Chen, W. Yan (Eds.), *Stud. Surf. Sci. Catal.*, Elsevier2007, pp. 499–505. doi: 10.1016/S0167-2991(07)80883-4.
- [60] M.G. O'Brien, A.M. Beale, C.R.A. Catlow, B.M. Weckhuysen, Unique organic-inorganic interactions leading to a structure-directed microporous aluminophosphate crystallization as observed with in situ raman spectroscopy, *J. Am. Chem. Soc.* 128 (36) (2006) 11744–11745, <https://doi.org/10.1021/ja064230a>.
- [61] Y. Wang, M. Lin, A. Tuel, Hollow TS-1 crystals formed via a dissolution–recrystallization process, *Microporous Mesoporous Mater.* 102 (1) (2007) 80–85, <https://doi.org/10.1016/j.micromeso.2006.12.019>.
- [62] D.Y. Xi, Q.M. Sun, J. Xu, M. Cho, H.S. Cho, S. Asahina, Y. Li, F. Deng, O. Terasaki, J.H. Yu, In situ growth-etching approach to the preparation of hierarchically macroporous zeolites with high MTO catalytic activity and selectivity, *J. Mater. Chem. A* 2 (42) (2014) 17994–18004, <https://doi.org/10.1039/c4ta03030c>.
- [63] Z. Qin, G. Melinte, J.P. Gilson, M. Jaber, K. Bozhilov, P. Boullay, S. Mintova, O. Ersen, V. Valtchev, The mosaic structure of zeolite crystals, *Angew. Chem. Int. Ed.* 55 (48) (2016) 15049–15052, <https://doi.org/10.1002/anie.201608417>.
- [64] J.C. Groen, T. Bach, U. Ziese, A.M. Paulaime-van Donk, K.P. de Jong, J.A. Moulijn, J. Pérez-Ramírez, Creation of hollow zeolite architectures by controlled desilication of Al-zoned ZSM-5 crystals, *J. Am. Chem. Soc.* 127 (31) (2005) 10792–10793, <https://doi.org/10.1021/ja052592x>.
- [65] Y. Wang, A. Tuel, Nanoporous zeolite single crystals: ZSM-5 nanoboxes with uniform intracrystalline hollow structures, *Microporous Mesoporous Mater.* 113 (1) (2008) 286–295, <https://doi.org/10.1016/j.micromeso.2007.11.027>.
- [66] D. Verboekend, M. Milina, J. Perez-Ramirez, Hierarchical silicoaluminophosphates by postsynthetic modification: influence of topology, composition, and silicon distribution, *Chem. Mater.* 26 (15) (2014) 4552–4562, <https://doi.org/10.1021/cm501774s>.
- [67] Y. Qiao, M. Yang, B. Gao, L. Wang, P. Tian, S. Xu, Z. Liu, Creation of hollow SAPO-34 single crystals via alkaline or acid etching, *Chem. Commun.* 52 (33) (2016) 5718–5721, <https://doi.org/10.1039/c5cc10070d>.
- [68] E.M. Flanigen, R.L. Patton, S.T. Wilson, Structural, synthetic and physicochemical concepts in aluminophosphate-based molecular sieves, in: P.J. Grobet, W.J. Mortier, E.F. Vansant, G. Schulz-Ekloff (Eds.), *Stud. Surf. Sci. Catal.*, Elsevier1988, pp. 13–27. doi: 10.1016/S0167-2991(09)60578-4.
- [69] J.Y. Li, J.H. Yu, R.R. Xu, Progress in heteroatom-containing aluminophosphate molecular sieves, *Proc. R. Soc. A* 468 (2143) (2012) 1955–1967, <https://doi.org/10.1098/rspa.2012.0058>.
- [70] J. Li, A. Corma, J. Yu, Synthesis of new zeolite structures, *Chem. Soc. Rev.* 44 (20) (2015) 7112–7127, <https://doi.org/10.1039/C5CS00023H>.